

**2023 NDIA MICHIGAN CHAPTER  
GROUND VEHICLE SYSTEMS ENGINEERING  
AND TECHNOLOGY SYMPOSIUM  
<AMM> TECHNICAL SESSION  
AUGUST 15-17, 2023 - NOVI, MICHIGAN**

## **Scan Sequence Optimization for Reduced Residual Stress and Distortion in LPBF Additive Manufacturing – An AISI 316L Case Study**

**Chuan He<sup>1</sup>, Chinedum E. Okwudire<sup>1\*</sup>**

<sup>1</sup>Department of Mechanical Engineering, University of Michigan, Ann Arbor, MI

### **ABSTRACT**

*Laser powder bed fusion (LPBF) additive manufacturing often results in defective parts due to non-uniform temperature distribution during fabrication. To mitigate this issue, the authors recently introduced SmartScan, an intelligent method that employs modeling and optimization to generate scan sequences that improve temperature uniformity. However, the previous version of SmartScan could only be applied to single layers. This paper presents an extension of SmartScan to three-dimensional parts by adjusting the thermal model and optimization objective. Through simulations and experiments involving fabricating AISI 316L stainless steel parts, the study demonstrates that the proposed SmartScan approach significantly improves temperature uniformity, reduces part distortion, and mitigates residual stress, as compared to conventional heuristic sequences.*

**Citation:** C. He, C. E. Okwudire, “Scan Sequence Optimization for Reduced Residual Stress and Distortion in PBF Additive Manufacturing – An AISI 316L Case Study,” In *Proceedings of the Ground Vehicle Systems Engineering and Technology Symposium (GVSETS)*, NDIA, Novi, MI, Aug. 15-17, 2023.

### **1. INTRODUCTION**

Laser powder bed fusion (LPBF) is an increasingly popular additive manufacturing (AM) technique for metals and other materials. In contrast to other metal AM technologies, LPBF involves depositing a layer of metal powder onto the build substrate and selectively melting it using a high-powered laser as a thermal energy input. The build chamber is then lowered, and a new layer of powder is added, enabling the production of parts with intricate features at relatively high tolerances [1]–[4]. However, the non-uniformity of the printed part's

temperature during LPBF production can heighten the probability of defects in the final product, including residual stresses, deformation, and other imperfections [5]–[8]. Post-process heat treatment is frequently necessary to alleviate these defects, but this approach can increase time and cost and does not remedy deformation or cracking caused by residual stresses prior to being relieved [9]. As a result, it is desirable to minimize the temperature gradient during the printing process to avoid residual stresses and related defects as much as possible.

Previous investigations have demonstrated that scanning methodologies have a significant impact on attaining a more uniform distribution of temperature. These methodologies consist of various approaches to select scanning process parameters, such as laser power, scanning speed, hatch spacing, scan pattern, and scan sequence [5], [9]–[18]. This manuscript specifically focuses on optimizing the scan sequence, i.e., the order in which a predetermined scan pattern is traced. Studies have indicated that the scan sequence substantially influences the temperature distribution in LPBF [7], [19]–[23]. However, heuristic scan sequences, which are widely utilized in practice, have significant weaknesses since they generally rely on geometric relationships that inadequately represent the impact of temperature distribution physics, leading to suboptimal thermal distribution. To address this shortcoming, our earlier work [19], [21]–[23] introduced an intelligent approach known as SmartScan, which is based on physics models for optimizing scan sequences for both single-laser and multi-laser systems. Experiments involving laser marking of stainless steel plates have demonstrated that SmartScan can greatly improve temperature homogeneity and decrease part deformation. Nonetheless, the previous version of SmartScan was only suitable for single-layer scanning and did not accommodate multi-layer part-scale printing.

To overcome the aforementioned deficiency of our earlier research, this manuscript modifies the formulation of SmartScan to enable it to handle geometries that are three-dimensional. Evaluations are carried out using simulations and experiments that involve the production of cantilever beams from AISI 316L stainless steel powder.

The organization of this article is as follows: Section 2 provides an overview of SmartScan and outlines the methodology

used to enhance it for multi-layer geometries. Sections 3 and 4 present the outcomes of the simulations and experiments, respectively, followed by the conclusions and suggestions for future research in Section 5.

## 2. MULTI-LAYER SMARTSCAN

The fundamental objective of SmartScan is to optimize the scan sequence by utilizing a thermal model instead of relying on heuristics. Our initial implementation of SmartScan [19] utilized a simplified finite difference method (FDM) to discretize the heat diffusion equation. To keep the model uncomplicated, we assumed a solitary layer of LPBF on a substrate, as in Fig. 1(a). To simplify the physics model, we excluded certain aspects of the melting pool thermal phenomena, such as latent heat effects, radiative heat transfer, and other melt pool phenomena. The model only incorporated conductive and convective heat transfer, which represented the thermal transfer between the layer, substrate, and their surroundings. This simplified model was designed to simulate the re-scanning process in LPBF [24].

However, the simplified thermal model used in our prior work [19] is not applicable to multi-layer components. As a result, a multi-layer element creation process is required to model the thermal activity at the part scale. Boundary conditions include heat convection between the uppermost layer and the ambient air, conduction between the lowermost layer and the substrate, and heat conduction between the part's sides, and the powder is neglected because the powder has relatively low thermal conductivity. The assumption is made that both the substrate temperature and ambient temperature remain constant; all material characteristics stay unchanged; and the powder that will be selectively scanned is considered as solid state due to extremely low thickness. The

corresponding model is illustrated in Fig. 1(b).

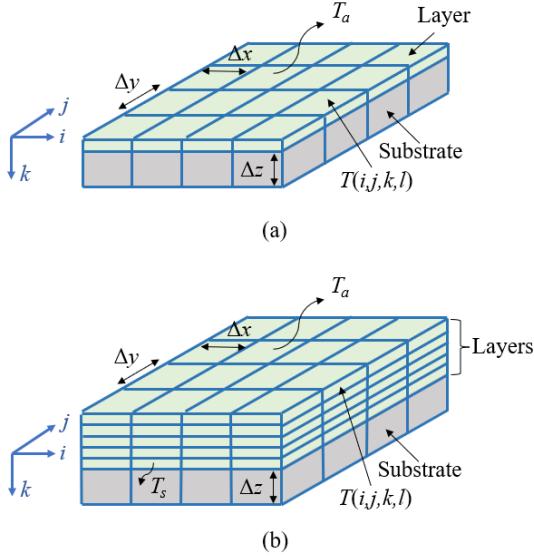


**Figure 1:** Simplified finite difference model of LPBF used for (a) single-layer SmartScan [19] and; (b) multi-layer SmartScan, where  $T_a$  represents the ambient temperature, and  $T_s$  represents the substrate temperature;  $\Delta x$ ,  $\Delta y$ , and  $\Delta z$  are the dimensions of each element.

The present research employs the same simplified FDM model as our earlier investigation [19], which can be formulated using the state equation.:

$$\mathbf{T}(l+1) = \mathbf{A}\mathbf{T}(l) + \mathbf{B}\mathbf{u}(l) \quad (1)$$

where  $\mathbf{T}(l)$  denotes the state vector that encompasses thermal information  $T(i,j,k)$  of all elements at time  $l$ . Matrix  $\mathbf{A}$  denotes the state matrix, while  $\mathbf{B}$  represents the input matrix. The sparse vector  $\mathbf{u}(l)$  signifies the power input, which only possesses non-zero values in the elements exposed to laser radiation. The impact of heat transfer through convection to an ambient temperature of  $T_a$ , utilizing the convection coefficient  $h$ , and through conduction to a substrate temperature of  $T_s$  are integrated into the model in Eq. (1) using a heat sink method [25]. The methodology supposes that it takes roughly  $n_p$  time steps to scan all features. The corresponding representation of the state-

space at the feature level can be formulated as follows:

$$\begin{aligned} \mathbf{T}(l_p + 1) &= \mathbf{A}_p \mathbf{T}(l_p) + \mathbf{b}; \\ \mathbf{A}_p &\triangleq \mathbf{A}^{n_p}; \mathbf{b} \triangleq \sum_{m=0}^{n_p-1} \mathbf{A}^m \mathbf{B} \mathbf{u}(m); l_p = n_p l \end{aligned} \quad (2)$$

To enhance the scan sequence, the temperature uniformity metric  $R(l_p)$  introduced in Ref. [19] is minimized

$$\begin{aligned} R(l_p) &= \sqrt{\frac{\sum_{i,j,k} (T(i,j,k,l_p) - T_{avg}(l_p))^2}{s T_m^2}} \\ R(l_p) &= \|\widehat{\mathbf{C}}\mathbf{T}(l_p)\|_2; \widehat{\mathbf{C}} = \frac{1}{\sqrt{s} T_m} \left[ \mathbf{I} - \frac{\mathbf{1}\mathbf{1}^T}{s} \mathbf{0} \right] \end{aligned} \quad (3)$$

where  $T_{avg}(l_p)$  signifies the mean temperature of elements  $T(i,j,k,l_p)$  at time  $l_p$ ,  $s$  represents the number of elements (after model reduction using radial basis functions), and  $T_m$  is the melting point of the material. In the case of a multi-layer part-scale problem, the state-space representation in Eq. (1) and Eq. (2) and the optimization objective in Eq. (3) for the  $n$ th layer are limited to the solidified portions of the topmost  $\min(c,n)$  layers as in Fig. 2, where  $c$  is a predefined constant value. The lower layers are excluded from the state-space equation and the corresponding objective function by assuming that it has reached a constant temperature value for the following reasons:

1. To reduce the model size and improve computational efficiency.
2. The topmost layers of the solidified portion experience more rapid temperature changes due to the energy input that causes residual stress and distortion.

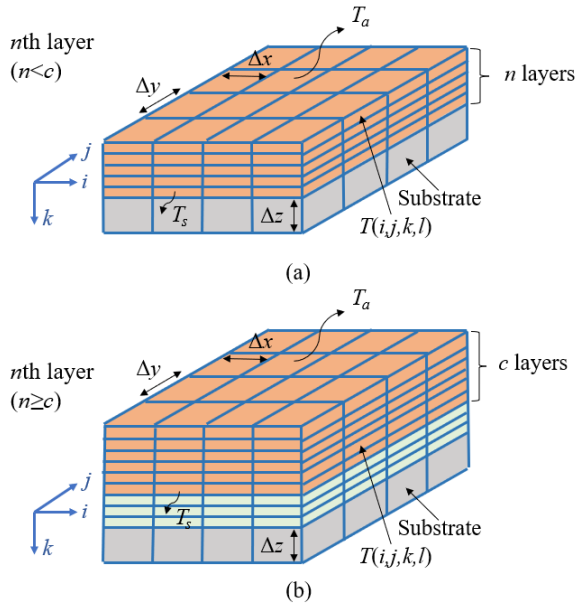


**Figure 2:** The portion of elements that contribute to the state-space equation and optimization target marked in orange when optimizing  $n$ th layer when (a)  $n < c$ ; (b)  $n \geq c$ .

Given the reduced element space that contributes to both the state space equation and optimization objective (see Fig. 2), the optimization problem for scan sequence in the  $n$ th layer considers the topmost  $\min(c, n)$  layers and can be formulated as follows

$$\begin{aligned} \min_{\hat{\mathbf{u}}(l_p)} \left( R(l_p + 1) = \|\widehat{\mathbf{C}}\mathbf{T}(l_p + 1)\|_2 \right) \\ \text{s.t. } \mathbf{T}(l_p + 1) = \widehat{\mathbf{A}}\mathbf{T}(l_p) + \widehat{\mathbf{B}}\hat{\mathbf{u}}(l_p) \end{aligned} \quad (4)$$

where  $\widehat{\mathbf{A}} = \mathbf{A}_p$ , the columns of  $\widehat{\mathbf{B}}$  represent the corresponding  $\mathbf{b}$  vectors as in Eq. (2) for each feature, and  $\hat{\mathbf{u}}(l_p)$  is a vector with only one element equal to 1 and all other elements equal to 0. The location of 1 in  $\hat{\mathbf{u}}(l_p)$  represents the column of  $\widehat{\mathbf{B}}$  and, consequently, the feature to be scanned.

The optimization function's objective, as shown in Eq. (4), can be reformulated as follows:

$$\begin{aligned} & \|\widehat{\mathbf{C}}\mathbf{T}(l_p + 1)\|_2^2 \\ &= \|\widehat{\mathbf{C}}\mathbf{A}\mathbf{T}(l_p) + \widehat{\mathbf{C}}\widehat{\mathbf{B}}\hat{\mathbf{u}}(l_p)\|_2^2 \\ &= \hat{\mathbf{u}}^T(l_p) \widehat{\mathbf{B}}^T \widehat{\mathbf{C}}^T \widehat{\mathbf{C}} \widehat{\mathbf{B}} \hat{\mathbf{u}}(l_p) \\ & \quad + 2\mathbf{T}^T(l_p) \widehat{\mathbf{A}}^T \widehat{\mathbf{C}}^T \widehat{\mathbf{C}} \widehat{\mathbf{B}} \hat{\mathbf{u}}(l_p) \\ & \quad + \mathbf{T}^T(l_p) \widehat{\mathbf{A}}^T \widehat{\mathbf{C}}^T \widehat{\mathbf{C}} \mathbf{A} \mathbf{T}(l_p) \end{aligned} \quad (5)$$

The optimization problem for the  $n$ th layer can be then reformulated as

$$\begin{aligned} \min_i \lambda_i \\ \text{s.t. } \lambda_i = \Gamma(i, i) + \Lambda(i, :) \mathbf{T}(l_p), i \in \{1, 2, \dots, n_f\} \end{aligned} \quad (6)$$

where  $\Gamma \triangleq \widehat{\mathbf{B}}^T \widehat{\mathbf{C}}^T \widehat{\mathbf{C}} \widehat{\mathbf{B}}$  and  $\Lambda \triangleq 2\widehat{\mathbf{B}}^T \widehat{\mathbf{C}}^T \widehat{\mathbf{C}} \widehat{\mathbf{A}}$ , and  $n_f$  denotes the number of features in  $n$ th layer. Moreover, the  $i$ th diagonal element of matrix  $\Gamma$  is represented by  $\Gamma(i, i)$ , while the  $i$ th row of matrix  $\Lambda$  is referred to as  $\Lambda(i, :)$ .

The summary of the procedure for identifying the optimal scanning sequence for  $n$ th layer is similar to the original SmartScan [19] depicted in Figure 3.

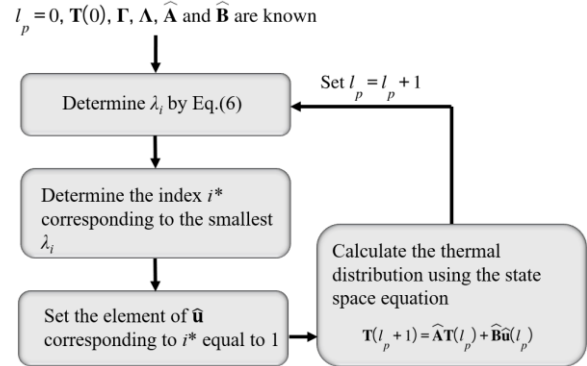


**Figure 3:** Flowchart of the SmartScan for  $n$ th layer

**Remark 1:** To facilitate the utilization of parallel computing for substantially improving the efficiency of optimization, it is presumed that the initial state of topmost  $\min(c, n)$  layers is at uniform thermal distribution and same value as the substrate temperature due to prolonged interlayer time. Thus, the optimization process of each layer can be independent and simultaneously executed as an individual task.

### 3. SIMULATIONS

This section showcases a simulation-based case study aimed at highlighting the efficacy of the proposed methodology in attaining a uniform distribution of temperature, in contrast to the widely used heuristic techniques documented in literature.

In this instance, two analogous models of cantilever beam shape were produced as described in Fig. 4 utilizing Stainless steel powder, type 316, 99.9% pure, -325 mesh particle size as the primary raw material. The model A has dimensions of 70 mm × 7 mm × 10 mm (L×W×H) while the model B is of dimensions of 100 mm × 10 mm × 12.5 mm (L×W×H). In contrast to the model A the model B has thinner teeth and a slimmer upper section, with an extended length. The experimental setup employed in the Section 4 is consistent with the simulation.

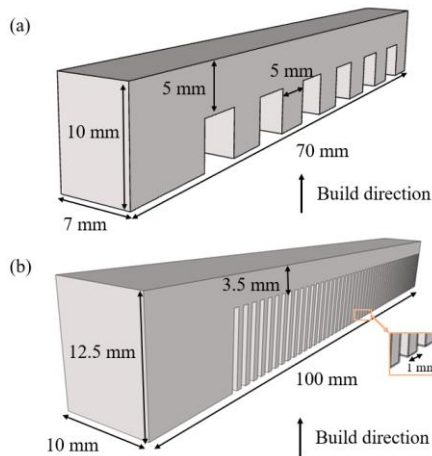


**Figure 4:** Cantilever beam geometry for case study of (a) model A; and (b) model B

In this study, the FDM model is composed of a maximum of twenty layers of elements, i.e.,  $c = 20$ , with each layer possessing a thickness of  $\Delta z = 50 \mu\text{m}$ . The element size for all layers is uniform, i.e.,  $\Delta x = \Delta y = 200 \mu\text{m}$ . The simulation employs a time step of 0.333

ms. In terms of boundary conditions, the upper surface undergoes convection, while the lower surface experiences conduction. However, the peripheral surfaces' heat conduction is disregarded. Furthermore, the chosen scanning pattern for both model A and model B is a bidirectional stripe pattern. Specifically, model A employs an angle rotation of 90 degrees between layers, whereas model B employs an angle rotation of 0 degrees. The infilled scanning stripes and their corresponding labels are illustrated in Fig. 5(a) and Fig. 5(b), respectively. The parameters utilized in the model are presented in Tab. 1, and for simplicity, are assumed to be constant, even though they vary with temperature in reality. The parameters listed in the table correspond to those employed in the experimental analysis described in Section 4.

**Table 1.** Parameters used in simulations (and experiments).

Parameter, symbol (Units)	Value
Laser power (W)	200
Laser spot diameter ( $\mu\text{m}$ )	77
Absorptance	0.37
Mark/scan speed (mm/s)	600
Conductivity (W/(mK))	22.5
Diffusivity ( $\text{m}^2/\text{s}$ )	$5.632 \times 10^{-6}$
Melting temperature (K)	1658
Convection coefficient (W/( $\text{m}^2\text{K}$ ))	25
Hatching distance ( $\mu\text{m}$ )	200
Initial temperature (K)	293
Ambient temperature (K)	293

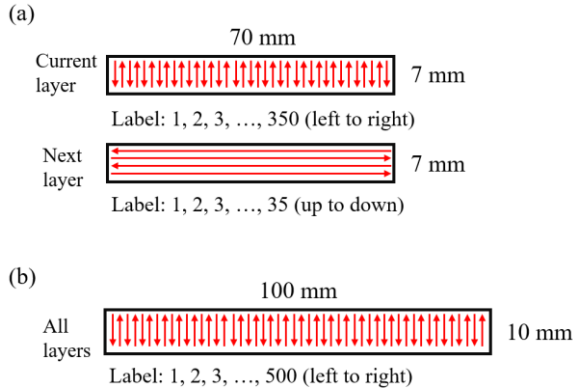


**Figure 5:** Scan pattern for case study of (a) model A; and (b) model B

For both cases A and B, the layers to be scanned are partitioned into sequentially numbered horizontal or vertical stripes, as illustrated in Fig. 5. In case A, the optimal scan sequence generated by SmartScan is compared to the commonly used Sequential (1, 2, 3, ..., end) heuristic sequence. Conversely, in case B, SmartScan is compared to three heuristic sequences, namely, Sequential (1, 2, 3, ..., end), Alternating (1, 3, ..., end-1, 2, 4, ..., end) and Out-to-in (1, end, 2, end-1, ..., end/2, end/2+1) approaches where *end* refers to the label of the last stripe.

As depicted in Fig. 6, for case A, each sequence's temperature uniformity metric, *R*, is presented as a function of the percentage of scanned stripes, accompanied by the corresponding mean value in parentheses. The proposed approach achieves mean *R* values that are 65.8% and 87.2% lower than those of the Sequential in layer 126 and 250, respectively. Layer 126 refers to the layer that is immediately above the teeth that includes overhang regions, while layer 250 denotes the topmost layer. Fig. 7 confirms this result by displaying the temperature distribution after 88, 175, 263, and 350 stripes are scanned for each approach. SmartScan is shown to positively impact the temperature distribution at all stages, thus providing validation for its effectiveness.

Scan Sequence Optimization for Reduced Residual Stress and Distortion in PBF Additive Manufacturing – An AISI 316L Case Study, C. He, et al.

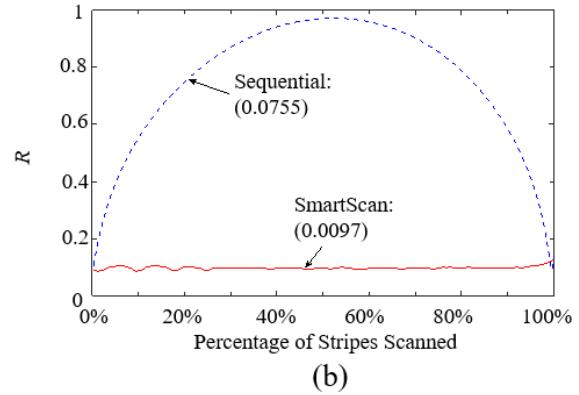
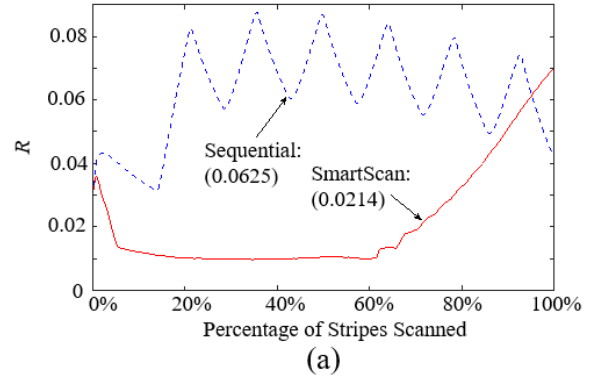


**Figure 6:** The thermal uniformity metric, *R*, for case A in (a) layer 126; and (b) layer 250 throughout the process

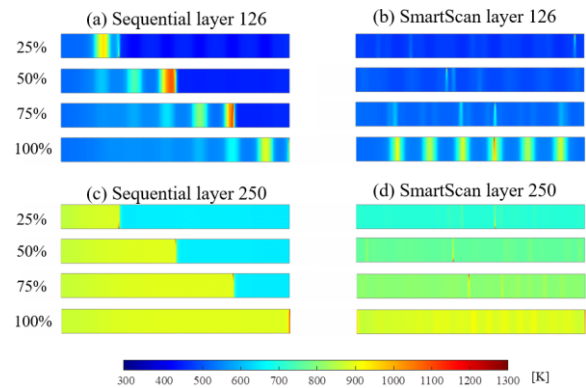


**Figure 7:** Simulated temperature distribution for case A at four instances during the scanning process using (a) Sequential in layer 126; (b) SmartScan in layer 250; (c) Sequential in layer 250; (d) SmartScan in layer 250.

As illustrated in Fig. 8, in case B, the temperature uniformity metric, *R*, for each scanning sequence is plotted as a function of the percentage of scanned stripes, along with

the corresponding mean value in parentheses). The proposed SmartScan approach achieves significantly lower mean  $R$  values, with reductions of 38.1%, 17.7% and 22.1% compared to the Sequential, Alternating and Out-to-in method in layer 200, respectively. Layer 200 refers to the layer in the middle portion of the upper beam. These findings are further supported by Fig. 9, which shows the temperature distribution after scanning 125, 250, 375, and 500 stripes.

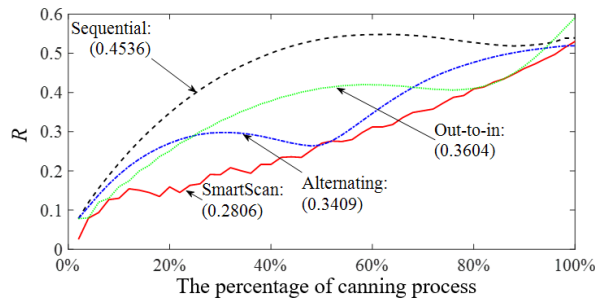


**Figure 8:** The thermal uniformity metric,  $R$ , for case B in layer 200 throughout the process

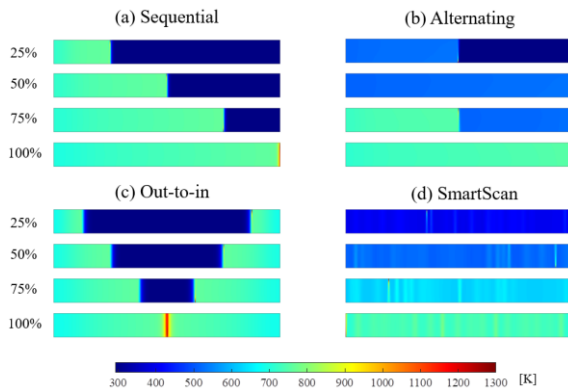


**Figure 9:** Simulated temperature distribution in layer 200 for case B at four instances during the scanning process using (a) Sequential; (b) Alternating; (c) Out-to-in; (d) SmartScan sequences.

**Remark 2:** The computation of the optimal sequence requires approximately one minute for each layer using a computer equipped with an AMD Ryzen 9 5900X 12-Core Processor, AMD Radeon RX 6900 XT and 32GB of RAM. The computational time can be decreased by utilizing radial basis functions [19], however, this may result in a

decrease in simulation accuracy. The optimization process for each layer can be efficiently accomplished via parallel computing.

## 4. EXPERIMENTS

### 4.1. EXPERIMENTAL SETUP AND PROCEDURE

The two parts simulated in Section 3 were printed on the open-architecture PANDA 11 LPBF machine (manufactured by OpenAdditive, LLC, Beavercreek, OH), as depicted in Fig. 10(a). The machine allows for customization of scan pattern and sequence using the Open Machine Control software. In Case A, the thinner teeth of the cantilever beams were sawed off the build plate using a band saw, and the upper surface was scanned using the Romer Absolute Arm (Hexagon AB, Sweden) model #7525SI with a scanning accuracy of  $63 \mu\text{m}$ . In Case B, the experimental temperature data was acquired using the Optris PI 640 G7 IR camera. The upper surface roughness was derived from the height profile captured using the same Romer Absolute Arm scanner model. The residual stress was measured by X-ray Diffraction method using the Rigaku SmartLab XRD model and analyzed with PDLX software as in Fig. 10(b).

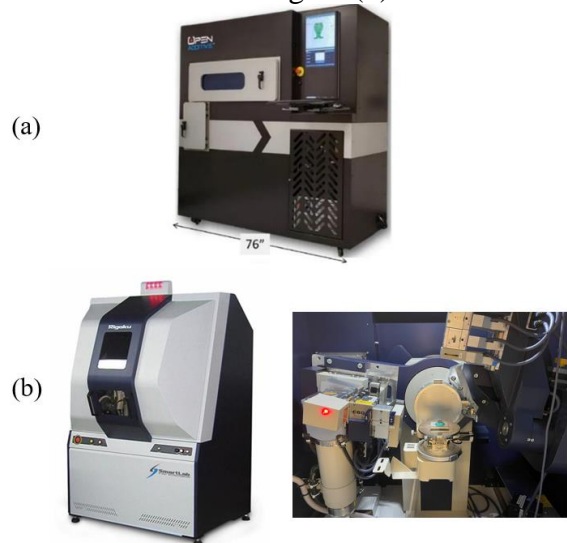


**Figure 10:** (a) PANDA 11 open architecture LPBF machine; and (b) Rigaku SmartLab XRD machine

## 4.2. RESULTS AND DISCUSSION

### 4.2.1 Case Study A

Illustrated in the Fig. 11, once the thinner tooth of the cantilever beams is removed by the band saw, the part experiences an upward deflection in response to the redistribution of the internal stress, which in turn predicts the eventual release of residual stress [26]. In Case A, the average and maximum deformation of the part are improved by 50.5% and 26.3%, respectively, with the implementation of approach SmartScan as compared to Sequential approach alone. Additionally, SmartScan incurs only 2.7% more printing time, indicating that it can effectively reduce thermal-induced deformation and residual stress without significantly sacrificing productivity.

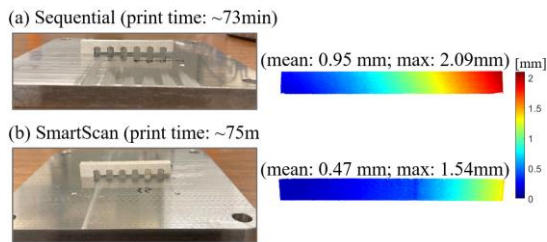


**Figure 11:** Fabricated cantilever beams and the scanned profile of their upper surface using (a) Sequential sequence; and (b) SmartScan approach.

### 4.2.2 Case B

A photograph of the actual printed parts is presented in Fig. 12. Each of the four cantilever beams are paired with a set of four sequences, namely Sequential, Alternating, Out-to-in and SmartScan, which are simultaneously fabricated on the same substrate. The enhancement in the uniformity in layer 200 of thermal distribution is validated by Fig. 13, which displays the experimentally obtained metric for thermal uniformity,  $R$ , and Fig. 14, which demonstrates the measured thermal

distribution at four different stages during scanning: i.e., with 25%, 50%, 75% and 100% of stripes scanned. The proposed SmartScan methodology, on average, achieves a superior thermal uniformity of 56.9%, 43.2%, and 35.9% as compared to the Sequential, Alternating, and Out-to-in approaches, respectively.

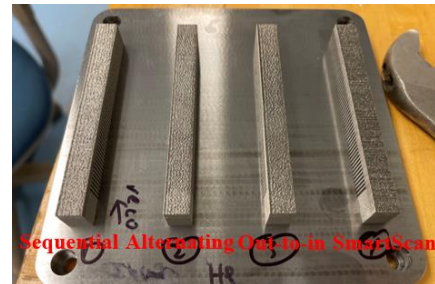


**Figure 12:** Fabricated cantilever beams using Sequential, Alternating, Out-to-in and SmartScan sequences, respectively.

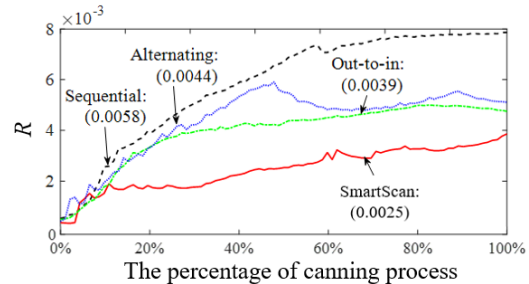


**Figure 13:** Experimentally determined thermal uniformity metric ( $R$ ) in layer 200 for different scan sequences as a function of the percentage of scanning process. The numbers in parentheses show the mean value of  $R$  for each scan sequence

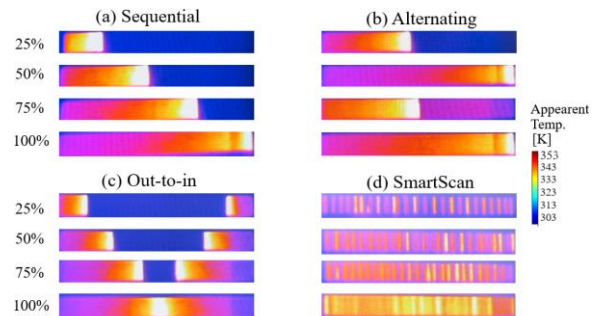


**Figure 14:** Experimentally determined temperature distribution in layer 200 at four instances during the scanning process.

Fig. 15 illustrates the height profile of the upper surface of each cantilever beam and the average roughness of the surfaces,  $R_a$ , is indicated at the ends and midpoint. The mean  $R_a$  values at the three points are also reported. It is observed that SmartScan has the poorest surface roughness among the four approaches, with a 11.4%, 9.9%, 8.0% increase in roughness compared to Sequential, Alternating and Out-to-in sequences, respectively. However, we observe a bias in surface roughness toward the left end of each beam, indicating a systematic source of surface roughness that needs to be investigated.

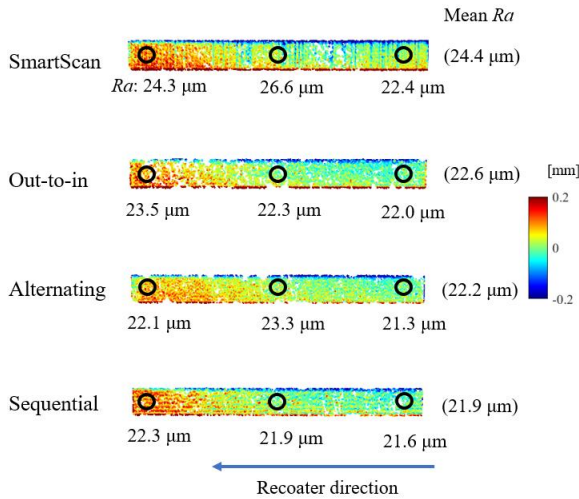


**Figure 15:** Experimentally scanned height profile of the top surface for different scan sequences; and the average roughness,  $R_a$ , at three spots for each cantilever beam.

Towards the end of each scan cantilever beam, residual stress primarily in the x-direction, is measured via XRD, as depicted in Fig. 16. This is attributed to the fact that the scan sequence significantly influences the stress in the perpendicular direction to the scanning vector [27]. Furthermore, there is a 84.7%, 88.9%, and 78.4% reduction in residual stress through the implementation of SmartScan compared to Sequential, Alternating, and Out-to-in sequences, respectively, suggesting its pivotal role in mitigating residual stress. The observed

scatter in stress measurements potentially signifies heterogeneity within the underlying microstructure, including grain size. Investigating these discrepancies represents a promising avenue for future research.

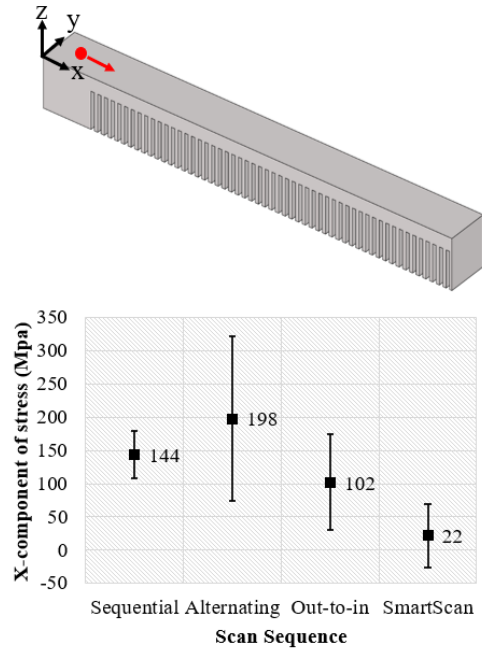


**Figure 16:** Residual stress and reliability determined by XRD at the specified location in x-direction (marked as red spot and red arrow)

## 5. CONCLUSION AND FUTURE WORK

This paper presents advancements to the SmartScan approach, previously introduced by the authors [19], enabling its application to 3D part-scale problems. Modifications to the thermal model and optimization objective were implemented to accommodate multiple layers while ensuring computational efficiency. A comparison was drawn between the impact of this approach and traditional heuristic sequences on the temperature distribution and mechanical properties of AISI 316L stainless steel part fabrication. Both simulation and experimental results demonstrated significant improvements in thermal uniformity and reduction of deformation and residual stress. Future research endeavors will focus on

manufacturing complex shapes for three-dimensional parts, as well as the exploration of SmartScan's influence on microstructure, porosity, and other properties and defects that may be indirectly affected by scan sequence.

## 6. ACKNOWLEDGMENT

The authors would like to thank Mr. Metin Kayitmazbatir and Prof. Miki Banu at the University of Michigan for their assistance with laser scanning of the parts and Ms. Ying Qi for her technical support with the XRD machine in the reported experiments.

## 7. REFERENCES

- [1] D. Herzog, V. Seyda, E. Wycisk, and C. Emmelmann, "Additive manufacturing of metals," *Acta Mater*, vol. 117, pp. 371–392, Sep. 2016, doi: 10.1016/j.actamat.2016.07.019.
- [2] W. J. Sames, F. A. List, S. Pannala, R. R. Dehoff, and S. S. Babu, "The metallurgy and processing science of metal additive manufacturing," *International Materials Reviews*, vol. 61, no. 5, pp. 315–360, Jul. 2016, doi: 10.1080/09506608.2015.1116649.
- [3] W. E. King *et al.*, "Laser powder bed fusion additive manufacturing of metals; physics, computational, and materials challenges," *Appl Phys Rev*, vol. 2, no. 4, p. 041304, Dec. 2015, doi: 10.1063/1.4937809.
- [4] L. E. Murr *et al.*, "Metal Fabrication by Additive Manufacturing Using Laser and Electron Beam Melting Technologies," *J Mater Sci Technol*, vol. 28, no. 1, pp. 1–14, Jan. 2012, doi: 10.1016/S1005-0302(12)60016-4.
- [5] G. Tapia and A. Elwany, "A Review on Process Monitoring and Control in Metal-Based Additive Manufacturing," *J Manuf Sci Eng*, vol. 136, no. 6, Dec. 2014, doi: 10.1115/1.4028540.
- [6] L. Parry, I. A. Ashcroft, and R. D. Wildman, "Understanding the effect of laser scan strategy on residual stress in selective laser melting through thermo-mechanical simulation," *Addit Manuf*, vol. 12, pp. 1–15, Oct. 2016, doi: 10.1016/j.addma.2016.05.014.
- [7] L. Mugwagwa, D. Dimitrov, S. Matope, and I. Yadroitsev, "Evaluation of the impact of scanning strategies on residual stresses in selective laser melting," *The International Journal of Advanced Manufacturing Technology*, vol. 102, no. 5–8, pp. 2441–2450, Jun. 2019, doi: 10.1007/s00170-019-03396-9.
- [8] J. Robinson, I. Ashton, P. Fox, E. Jones, and C. Sutcliffe, "Determination of the effect of scan strategy on residual stress in laser powder bed fusion additive manufacturing," *Addit Manuf*, vol. 23, pp. 13–24, Oct. 2018, doi: 10.1016/j.addma.2018.07.001.
- [9] Q. Chen *et al.*, "Island scanning pattern optimization for residual deformation mitigation in laser powder bed fusion via sequential inherent strain method and sensitivity analysis," *Addit Manuf*, vol. 46, p. 102116, Oct. 2021, doi: 10.1016/j.addma.2021.102116.
- [10] C. Reiff, W. Bubeck, D. Krawczyk, M. Steeb, A. Lechler, and A. Verl, "Learning Feedforward Control for Laser Powder Bed Fusion," *Procedia CIRP*, vol. 96, pp. 127–132, 2021, doi: 10.1016/j.procir.2021.01.064.
- [11] R. Wang, B. Standfield, C. Dou, A. C. Law, and Z. J. Kong, "Real-time process monitoring and closed-loop control on laser power via a customized laser powder bed fusion platform," *Addit Manuf*, vol. 66, p. 103449, Mar. 2023, doi: 10.1016/j.addma.2023.103449.
- [12] S. I. Kim and A. J. Hart, "A spiral laser scanning routine for powder bed fusion inspired by natural predator-prey behaviour," *Virtual Phys Prototyp*, vol. 17, no. 2, pp. 239–255, Apr. 2022, doi: 10.1080/17452759.2022.2031232.
- [13] Y. Liu *et al.*, "An optimized scanning strategy to mitigate excessive heat accumulation caused by short scanning lines in laser powder bed fusion process," *Addit Manuf*, vol. 60, p. 103256, Dec. 2022, doi: 10.1016/j.addma.2022.103256.
- [14] M. Boissier, G. Allaire, and C. Tournier, "Time Dependent Scanning Path Optimization for the Powder Bed Fusion Additive Manufacturing Process," *Computer-*

- Aided Design*, vol. 142, p. 103122, Jan. 2022, doi: 10.1016/j.cad.2021.103122.
- [15] M. Qin *et al.*, “Adaptive toolpath generation for distortion reduction in laser powder bed fusion process,” *Addit Manuf*, vol. 64, p. 103432, Feb. 2023, doi: 10.1016/j.addma.2023.103432.
- [16] D. Ramos, F. Belblidia, and J. Sienz, “New scanning strategy to reduce warpage in additive manufacturing,” *Addit Manuf*, vol. 28, pp. 554–564, Aug. 2019, doi: 10.1016/j.addma.2019.05.016.
- [17] M. Mani, B. M. Lane, M. A. Donmez, S. C. Feng, and S. P. Moylan, “A review on measurement science needs for real-time control of additive manufacturing metal powder bed fusion processes,” *Int J Prod Res*, vol. 55, no. 5, pp. 1400–1418, Mar. 2017, doi: 10.1080/00207543.2016.1223378.
- [18] Q. Wang, P. (Pan) Michaleris, A. R. Nassar, J. E. Irwin, Y. Ren, and C. B. Stutzman, “Model-based feedforward control of laser powder bed fusion additive manufacturing,” *Addit Manuf*, vol. 31, p. 100985, Jan. 2020, doi: 10.1016/j.addma.2019.100985.
- [19] K. S. Ramani, C. He, Y.-L. Tsai, and C. E. Okwudire, “SmartScan: An Intelligent Scanning Approach for Uniform Thermal Distribution, Reduced Residual Stresses and Deformations in PBF Additive Manufacturing,” *Addit Manuf*, p. 102643, Feb. 2022, doi: 10.1016/j.addma.2022.102643.
- [20] J. P. Kruth, L. Froyen, J. van Vaerenbergh, P. Mercelis, M. Rombouts, and B. Lauwers, “Selective laser melting of iron-based powder,” *J Mater Process Technol*, vol. 149, no. 1–3, pp. 616–622, Jun. 2004, doi: 10.1016/j.jmatprotec.2003.11.051.
- [21] C. He, K. S. Ramani, and C. E. Okwudire, “An intelligent scanning strategy (SmartScan) for improved part quality in multi-laser PBF additive manufacturing,” *Addit Manuf*, vol. 64, p. 103427, Feb. 2023, doi: 10.1016/j.addma.2023.103427.
- [22] C. He, Y.-L. Tsai, and C. E. Okwudire, “A Comparative Study on the Effects of an Advanced Scan Pattern and Intelligent Scan Sequence on Thermal Distribution, Part Deformation, and Printing Time in PBF Additive Manufacturing,” *Proceedings of the ASME 2022 17th International Manufacturing Science and Engineering Conference (MSEC). Volume 1: Additive Manufacturing; Biomanufacturing; Life Cycle Engineering; Manufacturing Equipment and Automation; Nano/Micro/Meso Manufacturing*, Jun. 2022, doi: 10.1115/MSEC2022-85301.
- [23] C. He, K. S. Ramani, Y.-L. Tsai, and C. E. Okwudire, “A Simplified Scan Sequence Optimization Approach for PBF Additive Manufacturing of Complex Geometries,” in *2022 IEEE/ASME International Conference on Advanced Intelligent Mechatronics (AIM)*, Jul. 2022, pp. 1004–1009. doi: 10.1109/AIM52237.2022.9863375.
- [24] H. Ali, H. Ghadbeigi, and K. Mumtaz, “Effect of scanning strategies on residual stress and mechanical properties of Selective Laser Melted Ti6Al4V,” *Materials Science and Engineering: A*, vol. 712, pp. 175–187, Jan. 2018, doi: 10.1016/j.msea.2017.11.103.
- [25] J. Ning, D. E. Sievers, H. Garmestani, and S. Y. Liang, “Analytical Thermal Modeling of Metal Additive Manufacturing by Heat Sink Solution,” *Materials*, vol. 12, no. 16, p. 2568, Aug. 2019, doi: 10.3390/ma12162568.
- [26] M. Yakout, M. A. Elbestawi, S. C. Veldhuis, and S. Nangle-Smith, “Influence of thermal properties on residual stresses in SLM of aerospace alloys,” *Rapid Prototyp J*, vol. 26, no. 1, pp. 213–222, Jan. 2020, doi: 10.1108/RPJ-03-2019-0065.
- [27] L. A. Parry, I. A. Ashcroft, and R. D. Wildman, “Geometrical effects on residual stress in selective laser melting,” *Addit Manuf*, vol. 25, pp. 166–175, Jan. 2019, doi: 10.1016/j.addma.2018.09.026.